HELLENIC REPUBLIC
National and Kapodistrian University of Athens

School of Science - Department of Physics

Program of Postgraduate Studies "Materials Physics"

Kinetics of radiation defects and carbon solute atoms in ion irradiated pure Fe

Syskaki Maria-Andromachi

Commitee Members:

Apostolopoulos George
Principal Researcher, NCSR «Demokritos»

Glenis Spiridon
Assistant Professor, Department of Solid State Physics

Mertzimekis Theodoros
Associate Professor, Department of Nuclear and Particle Physics

Athens 2019

Abstract

Ferritic/martensitic steels, i.e., Fe-rich alloys with bcc structure, based on the Fe-Cr-C system, are candidate structural materials for the construction of future fusion power plants, mainly because of their high resistance to radiation damage accumulation and their desirable mechanical properties. Carbon is a main alloying element in these steels playing a major role for the desirable mechanical properties, also under irradiation. Nevertheless, a deeper understanding of the behaviour of C under irradiation conditions is still required, as issues, such as the embrittlement during low temperature irradiation, need to be resolved for the successful implementation of these steels.

The present thesis focuses on the interaction between carbon atoms and radiation defects in α-iron, which is considered as a simple model system for the more complex ferritic steels. The aim of the investigation is to assess possible consequences of carbon/defect interactions to properties of steels under irradiation. The defects are generated during irradiation with a 5 MeV proton beam at cryogenic temperature (T$\sim$ 25 K). Defect evolution is observed during post-irradiation thermal annealing of the samples. The physical property used for the observation of defect evolution is the electrical resistivity, which is a sensitive indicator of changes in solute atom and defect concentrations.

Samples of pure and C-doped (220 at. ppm) α-iron were used in the experiments. A number of samples was irradiated at the 5.5 MV TANDEM Accelerator of NCSR "Demokritos", in the ion irradiation facility IR^2, to three dose levels between 0.5 and 4.5×10^{16} cm^{-2}. The irradiations were performed at cryogenic temperature of $T = 25$ K, where all defects are nearly immobile. Un-irradiated and irradiated samples were subjected to isochronal annealing by rapid ohmic self-heating in the temperature range $300 < T < 700$ K. The annealing temperature was increased in steps, ΔT, keeping a constant ratio of $\Delta T/T \approx 0.03$. At the end of each annealing interval, the sample was rapidly quenched in liquid helium (LHe) vapor and the electrical residual resistivity was measured always at the base temperature of $T = 4$ K by the standard DC four-probe method. The migration and annihilation of defects, as well as the migration of carbon solute atoms, was observed. The effect of carbon was assessed by comparing the annealing spectra of pure and carbon-doped samples in the un-irradiated and irradiated state, respectively.

The un-irradiated Fe-C alloys exhibit two resistivity recovery stages during isochronal annealing: A (440 K) and B (540 K). These have been also observed by previous authors and are attributed to C migration and precipitation of metastable ε-carbide and cementite, respectively.

In the irradiated Fe-C specimens the recovery stages IV_A and IV_B are observed at 330 K and $550 - 600$ K, respectively. The observation of stage IV_A is attributed to the interaction of C with irradiation defects to form complexes, most probably vacancy-C clusters. The presence of clusters retards the process of ε-carbide formation and this is why the stage A at 440 K is not observed in irradiated specimens. On the other hand the stage IV_B occurs at approximately the same temperature as stage B in un-irradiated Fe-C and thus it has the same origin, i.e., formation of cementite. However, at high irradiation doses this process is also affected by the formation of vacancy-C complexes and IV_B shifts to higher temperature.

Σύνοψη

Τα φερριτικά/μαρτενσιτικά ατσάλια με βάση το σύστημα Fe-Cr-C είναι αυτή τη στιγμή τα επικρατέστερα δομικά υλικά για τα μελλοντικά εργοστάσια παραγωγής ενέργειας μέσω της πυρηνικής σύντηξης. Κύρια χαρακτηριστικά τους είναι η υψηλή αντοχή σε συνθήκες ακτινοβόλησης και οι ικανοποιητικές μηχανικές τους ιδιότητες. Ο άνθρακας αποτελεί κύριο στοιχείο του κράματος στα ατσάλια αυτής της κατηγορίας και επηρεάζει σημαντικά τις επιθυμητές μηχανικές ιδιότητες, ακόμη και κατά την ακτινοβόληση. Αναντίρρητη ανάγκη αποτελεί η περαιτέρω μελέτη των ιδιοτήτων τους, ώστε να υπάρξει βαθύτερη κατανόηση της συμπεριφοράς τους σε συνθήκες ακτινοβόλησης, καθώς προβλήματα όπως η ψαθυροποίηση κατά την ακτινοβόληση σε χαμηλή θερμοκρασία μένουν ακόμη να επιλυθούν, για να καταστεί δυνατή η επιτυχής εφαρμογή τους.

Στα πλαίσια της παρούσας διπλωματική εργασίας μελετάται η αλληλεπίδραση μεταξύ των ατόμων άνθρακα και ατελειών από ακτινοβόληση στο κρυσταλλικό πλέγμα του χωροκεντρωμένου σιδήρου, ο οποίος μπορεί να θεωρηθεί ως ένα σύστημα αναφοράς που θα προσεγγίζει σε μεγάλο βαθμό την συμπεριφορά των πιο σύνθετων φερριτικών κραμάτων. Ο σκοπός αυτής της μελέτης αφορά την συσχέτιση των πιθανών επιπτώσεων της αλληλεπίδρασης των ατόμων άνθρακα με τις ατέλειες στις ιδιότητες των ατσαλιών κατά την ακτινοβόληση. Οι ατέλειες δημιουργούνται με ελεγχόμενο τρόπο κατά την ακτινοβόληση των δειγμάτων με πρωτόνια ενέργειας 5 MeV σε κρυογενική θερμοκρασία (~ 25 K). Η κινητική των ατελειών παρατηρείται κατά τη θερμική ανόπτηση των δειγμάτων. Η φυσική ποσότητα που χρησιμοποιείται για την παρατήρηση της εξέλιξης των ατελειών είναι η ηλεκτρική αντίσταση, η οποία αποτελεί ένα εξαιρετικά ευαίσθητο δείκτη των αλλαγών που συμβαίνουν στις συγκεντρώσεις ατελειών και προσμίξεων.

Δείγματα καθαρού σιδήρου και σιδήρου εμπλουτισμένου με άνθρακα (220 at. ppm) χρησιμοποιήθηκαν στα πειράματα. Ένας αριθμός δειγμάτων ακτινοβολήθηκε στον επιταχυντή TANDEM 5.5 MV του ΕΚΕΦΕ "Δημόκριτος", στην ειδικά σχεδιασμένη εγκατάσταση για ακτινοβόληση δειγμάτων με ιόντα IR^2, σε τρία επίπεδα δόσης μεταξύ 0.5 και 4.5×10^{16} cm^{-2}. Η ακτινοβόληση των δειγμάτων διεξήχθη σε κρυογενική θερμοκρασία $T = 25$ K, όπου όλες οι ατέλειες είναι σχεδόν ακίνητες. Στη συνέχεια, τα δείγματα, ακτινοβολημένα και μη, υποβάλλονται σε ισόχρονες θερμικές ανοπτήσεις μέσω απότομης ωμικής αυτοθέρμανσης στο εύρος θερμοκρασιών $300 < T < 700$ K. Η θερμοκρασία ανόπτησης αυξανόταν ελεγχόμενα και σταδιακά, σε βήματα ΔT, διατηρώντας σταθερό ρυθμό $\Delta T/T \approx 0.03$. Μετά το πέρας κάθε ανόπτησης, το δείγμα βυθιζόταν ακαριαία σε περιβάλλον υγρού ηλίου (LHe) και μετρούνταν η απομένουσα ηλεκτρική αντίσταση πάντα στη θερμοκρασία των $T = 4$ K με την καθιερωμένη μέθοδο των τεσσάρων επαφών. Έτσι, παρατηρούνται η δημιουργία, η μετανάστευση και η εξαφάνιση των ατελειών, αλλά και

η μετανάστευση των ατόμων άνθρακα στον κρύσταλλο. Τα διάφορα αυτά στάδια καταγράφονται και η επίδραση του άνθρακα εκτιμάται με σύγκριση των διαγραμμάτων του καθαρού και του εμπλουτισμένου σιδήρου.

Τα μη-ακτινοβολημένα δείγματα σιδήρου εμπλουτισμένου με άνθρακα παρουσιάζουν δύο στάδια αποκατάστασης της αντίστασης κατά την ισόθερμη ανόπτηση: Α (440 K) και Β (540 K). Αυτά τα στάδια αναφέρονται στη διεθνή βιβλιογραφία και αποδίδονται στη μετανάστευση του άνθρακα και στη δημιουργία του μετασταθούς καρβιδίου τύπου ε και του σεμεντίτη, αντίστοιχα.

Στα ακτινοβολημένα δείγματα σιδήρου εμπλουτισμένου με άνθρακα καταγράφονται τα στάδια IV_A και IV_B στους 330 K και στους $550 - 600$ K, αντίστοιχα. Το στάδιο IV_A αποδίδεται στην αλληλεπίδραση του άνθρακα με τις ατέλειες από ακτινοβόληση προς το σχηματισμό συμπλεγμάτων ατελειών, πιθανότατα ζευγών άνθρακα - πλεγματικού κενού. Η παρουσία τέτοιων συμπλεγμάτων καθυστερεί τη δημιουργία του καρβιδίου τύπου ε και έτσι δεν παρατηρείται το στάδιο Α στα ακτινοβολημένα δείγματα. Αντιθέτως, το στάδιο IV_B καταγράφεται στην ίδια περίπου θερμοκρασία με το στάδιο Β των μη ακτινοβολημένων δειγμάτων. Έτσι, θεωρούμε ότι έχουν κοινή προέλευση και συγκεκριμένα το σχηματισμό του σεμεντίτη. Ωστόσο, στα ακτινοβολημένα με υψηλή δόση δείγματα, αυτή η διεργασία επηρεάζεται από το σχηματισμό συμπλεγμάτων άνθρακα / πλεγματικών κενών, με αποτέλεσμα το στάδιο IV_B να μετατοπίζεται σε υψηλότερες θερμοκρασίες.

To my parents, Maria and Emmanuel.

Acknowledgments

First and foremost, I would like to express my deep sense of gratitude to my supervisor Dr. G. Apostolopoulos, Researcher at NCSR "Demokritos", who provided me with the opportunity to join his research team as a master student, and who gave me access to the laboratory and research facilities. I would also like to thank him for the patient guidance, the useful comments and the enlightening remarks through the whole process of this master thesis. I spent more than a year working with the entire research team, who truly taught me how to be a team member. Their continuous support and encouragement, as well as their work ethics, made the whole task motivating and pleasant. Thank you for your constructive cooperation.

Moreover, I am sincerely thankful to Prof. S. Glenis, UoA, for the fruitful discussions regarding physics, as one of committee members. I am grateful to him for sharing expertise, and sincere and valuable guidance.

Also, I would also like to thank Prof. Th. Mertzimekis, UoA, for the actual support on the way, as one of committee members and for his insightful comments and encouragement.

I am particularly grateful to Dr. Z. Kotsina and Doctoral candidate A. Theodorou, two people who helped me all the way through this thesis. They were there for me every day for scientific and everyday's life matters. They have willingly shared their precious time and patience, especially during the process of experimental procedures. Without their precious support it would not be possible to conduct this research.

Special thanks and deep gratitude I feel for my mother and father, who have supported me throughout the entire process and encouraged me to face every difficulty.

Last but not least, I would like to thank my loved ones, who were by my side every day, both by keeping me harmonious and helping me putting pieces together. I will be grateful forever for your love.

Contents

Chapter 1

Introduction

1. Materials research for fusion

Nowadays people get more and more concerned about environmental issues and climate change, since it is already affecting life on our planet. Equally important is the fact that coal and oil supplies become depleted. Consequently, the need to use clean energy sources is day after day developing into the major issue that troubles not only the scientific community, but politicians and societies too. Replacing the existing power generation methods with renewable energy sources and nuclear power can be the key to solve the global environmental problem. When it comes to renewable energy sources, such as wind and hydroelectric power, together with solar energy, there are still many technological barriers for the time being that limit the renewable energy use to about 14% of the global use. On the other hand, nuclear power is becoming a favoured option for large-scale power generation. Fission power is facing safety issues and concerns about the disposal of radioactive waste. In contrast, fusion could become an energy solution in the near future, since it is zero emitting, safe and clean, with a plentiful supply of raw materials. There are only a few grams of fuel in the reactor vessel, which is sufficient for a few seconds of burn. Therefore, a runaway reaction is not possible. Recent advantages in plasma physics, simulation, engineering and materials are bringing us closer to making fusion energy a reality [1].

The nuclear fusion reaction between deuterium (^{2}H) and tritium (^{3}H):

$$^2\mathrm{H} + {}^3\mathrm{H} \rightarrow {}^3\mathrm{H}(3.5\mathrm{MeV}) + \mathrm{n}(14.1\mathrm{MeV}) \tag{1.1}$$

is the most promising one for commercial fusion power. The great challenge is

to sustain fusion for sufficient time, in order to make this process energy-efficient at competitive cost. This has been the subject of decades of worldwide research efforts. To achieve fusion, the Coulomb barrier must be penetrated, requiring plasma temperatures of about $2 \cdot 10^8$ K. Plasma-facing components must withstand extreme heat loads. Energy from fusion power will be extracted from the 14.1 MeV kinetic energy of the neutrons produced in the previous reaction. This kinetic energy must be converted to electricity by a conventional thermal power plant. Thus, suitable materials for a safe, reliable, commercial use of fusion power are the subject of research over the past decades.

Neutrons are very penetrating particles, being of neutral charge. They pass through most material, and hence they can strongly interact at very low energies. In fusion power plants, neutrons gradually slow down in the blanket and heat is generated from their kinetic energy. This heat is absorbed by liquid coolants, which enter the core at lower temperature and exits at higher temperature after collecting fusion energy. Therefore, the blanket must be capable of withstanding intense irradiation and heat loads for long periods. Substantial gaseous (H and He) and solid transmutation products can also be created during this process, which can speed up the embrittlement of materials. Equally important are the induced currents and magnetic fields, together with thermomechanical loads, which may lead to damaging stresses caused by Lorentz forces for the in-vessel components. All things considered, fusion materials demand superior mechanical performance for the optimal operation, preventing maintenance shutdowns.

The study of the effects of irradiation on a material's microstructure and properties combines computational materials science and experimental validation. Some of the different lines of research are the structural materials with advanced radiation tolerance for the blanket, the liquid-metal coolants for advanced in-vessel components and the neutron multipliers and ceramic breeders for efficient tritium fuel production.

Facilities with a fusion-relevant neutron source for materials testing are expected to be available in the near future. This is an essential pending step in fusion roadmaps, considering the need for investigating materials science phenomena combined with collecting data for ab initio designing of fusion reactors. Testing facilities with a 14.1 MeV neutron source for irradiating candidate materials under fusion-reactor conditions and offering control of the temperature of the irradiated material are going to pave the way for defining the suitability of a material for nuclear applications in fusion reactors [2].

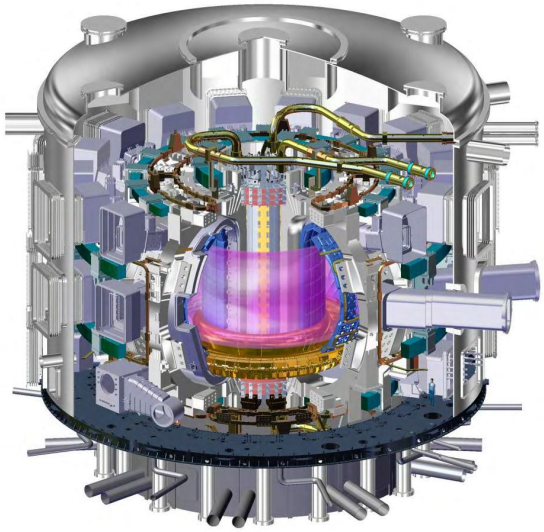

Figure 1.1: Schematic of the ITER fusion reactor.

2. Ferritic/Martensitic alloys for fusion

Iron at room temperature has body-centred cubic (bcc) structure and is called ferrite. Another name often used for ferrite is alpha iron or α-iron. At higher temperatures, the face-centred cubic (fcc) structure of iron appears, which is called austenite or γ-Fe. Steels may have either bcc or fcc structure at room temperature, depending on their composition, and they are characterized as ferritic or austenitic, respectively.

Martensite is named after the German metallurgist Adolf Martens and it refers to a metastable phase consisting of a supersaturated interstitial solid solution of carbon in a body-centered tetragonal iron form. It forms in carbon steels by very quick cooling of the austenite form of iron. This is used as a strengthening mechanism of the alloy. The rapid quenching at such high rate does not give enough time to the atoms to diffuse to new atomic positions. This causes a quick rearrangement of the atoms including a large number of dislocations, inducing a shear deformation from the face-centered cubic austenite to a highly strained body-centered tetragonal form, supersaturated with carbon. Thus, the austenite-to-martensite transformation is a diffusionless transformation. Martensite is a non-equilibrium, but an exceptionally hard phase of steel.

In the past decades, low- or reduced-activation ferritic/martensitic (RAFM) steels have been developed [3]. The activation of the structural materials in a fusion power plant has to be as low and quickly decaying as possible during operation,

maintenance shutdowns and disposal. Thus, the chemical composition of these materials should be based on low activation elements, such as Fe, Cr, V, Ti, W, Si and C.

Low activation ferritic-martensitic steels are considered as structural materials for fusion reactors. The advantages of these over other candidate materials are:

- high resistance to irradiation swelling
- favorable thermal properties
- adequate structural properties up to $T = 550°\mathrm{C}$
- improved safety and environmental features.

As favorable thermal properties, the better surface heat capability due to their lower coefficient of linear thermal expansion and higher coefficient of thermal conductivity is considered. However, their operational temperature range at present is $T = 350$ to $500°\mathrm{C}$. The low limit comes from the effects of irradiation-induced embrittlement, with an increase in ductile-to-brittle transition temperature (DBTT), while the upper limit emerges from a strong reduction in mechanical strength [4]. Research activities studying these limits will prove if RAFM steels can be used for fusion reactor's first wall, in a water-cooled ceramic tritium breeder system.

3. Point defects in solids

On an atomic scale, there is no perfect crystalline structure, excluding idealized solids. A crystalline defect refers to a lattice irregularity and is classified according to the geometry or dimensionality of the defect. Most often the crystal symmetry is interrupted by point defects, which are associated with one or two atomic positions. These kind of defects occur at or around a single lattice point. In Fig. 1.2, two types of point defects are shown. A vacancy is a lattice point, which is normally occupied, but from which an atom is missing. This is the simplest of the point defects and exists in almost all crystalline solids, since it is impossible to create a material free of defects.

An interstitial atom is located in space between the lattice points, which normally is not occupied. If it is the same kind of atom as the host atoms, then it is called self-interstitial, otherwise it is called interstitial impurity, as discussed in Fig

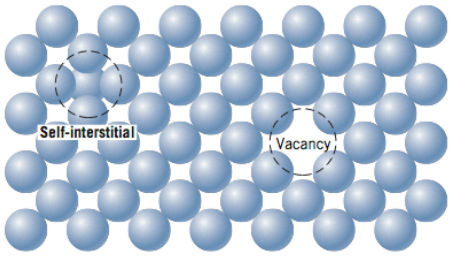

Figure 1.2: Two-dimensional schematic representations of vacancy and interstitial defects.

1.3. In metals, a self-interstitial introduces relatively large distortions in the surrounding lattice space, since the atom is larger than the interstitial space, where it is situated. Thus, the concentration of this kind of defects is significantly lower than that of vanancies. A close pair of an interstitial and a vacancy is called a Frenkel pair. It resembles an atom leaving its normal position from the lattice crystal and moving into the interstitial site.

Point defects can also be generated by irradiation. Heavy bombardment of a solid by energetic ions can displace atoms from their equilibrium positions. Several types of defects can be brought about by high-energy radiation centers. These defects are:

1. *Vacancies.* Vacant lattice sites can be created by collisions of energetic particles with the atoms in a crystal lattice. The energy transferred in these collisions is usually sufficient for the recoiling atom to create further vacant lattice sites by subsequent collisions. Thus, for each primary collision, a cascade of collisions is initiated resulting in vacancies.

2. *Interstitial atoms.* The atoms displaced from their equilibrium positions in the lattice can stay in an interstitial, or non-equilibrium, position, since they do not recombine immediately with a nearby vacancy.

3. *Impurity atoms.* Neutron bombardment can cause the formation of impurity atoms by transmutation. Moreover, fission products introduced by the fission process are often pronounced [5].

In addition to simple collisions, there are other important processes leading to observable radiation effects. These processes are:

1. *Replacement collisions.* If a collision between a moving particle and a stationary atom results in ejection of the stationary atom and leaves the interstitial

with insufficient kinetic energy for it to escape from the vacancy it has created, then it will fall into the vacancy, dissipating its kinetic energy through lattice vibrations as heat. The number of replacement collisions may exceed the number of displacement collisions for a reasonable choice of energy parameters. This can result in the interchange of moving atoms with lattice atoms, which can create observable effects in polyatomic materials.

2. *Thermal and displacement spikes.* When a particle is moving fast trough a lattice, or when an atom, that has been hit hard enough to vibrate with large amplitude without being displaced, will transfer energy to its neighbours, which become abnormally excited. Thus, the region of material around the track of a knocked-on atom will be rapidly heated. The region of excitation expands and there is a simultaneous drastic decrease of temperature. The result is called a thermal spike, that is rapid heating and quenching of a small volume of the material. When the energy of a fast moving atom falls below a transition value, which depends on the atomic number, the mean free path between displacement collisions becomes of the order of the atomic spacing. Then each collision results in a displacement atom and a displacement spike appears in this region of the material.

3. *Ionization effects.* The passage of charged particles trough a crystal latticemay cause extensive ionization and electronic excitation, which can lead to bond rupture, luminescence, etc. in many types of solids.

Impurity point defects found in solids are of two types: substitutional and interstitial. For the first type, the solute atoms replace or substitute for the host atoms. There are some conditions, which must be fulfilled, so that the former dissolves in the latter. In particular, the two atoms must have an atomic radii difference of less than about $\pm 15\%$, be of the same electronegativity. The crystal structures for metals must be the same for both atom types and other factors being equal, a metal will dissolve primarily a metal of higher valency than one of a lower.

For the second type, the defects are located in the void space between the host atoms. For metallic materials that have high atomic packing factors, interstitial void space is relatively small. Thus, the atomic diameter of interstitial impurities must be substantially smaller than that of the host atoms. So the maximum allowable concentration of interstitial impurity atoms is less than $\pm 10\%$.

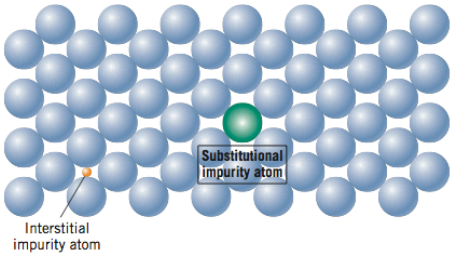

Figure 1.3: Two-dimensional schematic representations of substitutional and interstitial impurity atoms.

4. Point defect kinetics

As noted above, vacancies and interstitials are expected to interact with one another. In fact, they can annihilate each other by combining, or they can disappear at sinks (dislocations, surfaces, grain boundaries, etc.). In all of these processes there is a close analogy to chemical reactions, although the reaction rate is frequently limited by diffusion. In that sense, the following analysis on the chemical reaction aims to describe the annihilation by the recombination of interstitials and vacancies, as in the case of Frenkel pairs.

The way chemical reactions evolve is described by differential equations known as rate laws. A proposed mechanism is used in order to construct the rate law, which then is compared with experimental results for evaluation. Reaction rates depend on the composition and the temperature of the reaction mixture.

Considering a reaction of the form of:

$$2\mathrm{A} + \mathrm{B} \rightarrow \mathrm{C} + 3\mathrm{D} \tag{1.2}$$

where the reactants are A and B, the products are C and D. The rate of consumption of each of the reactants at a given time is:

$$-\frac{d[R]}{dt} \tag{1.3}$$

where [R] is the concentration of A or B and the formation of each of the products is:

$$\frac{d[P]}{dt} \tag{1.4}$$

where [P] is the concentration of C or D.

From the stoichiometry for the reaction, it follows:

$$\frac{d[C]}{dt} = \frac{1}{3}\frac{d[D]}{dt} = -\frac{1}{2}\frac{d[A]}{dt} = -\frac{d[B]}{dt} \tag{1.5}$$

In either case, there are several rates connected with one reaction. The rate of reaction is proportional to the concentrations of the reactants raised to a power. In case of:

$$\text{A} \rightarrow \text{B} \tag{1.6}$$

it would be with the concentration raised to the first power:

$$u = k[A] \tag{1.7}$$

The coefficient k is the rate constant and depends on the temperature.

Many reactions are found to have rate laws of the form

$$u = k[A]^a[B]^b... \tag{1.8}$$

depending on the stoichiometry of the reaction. The power to which the concentration of a reactant or a product is raised in the rate law is the order of the reaction with respect to it. Thus, the rate law of A is of a order. The overall order of the reaction is the sum of the individual orders ($a + b + ...$). Therefore, the rate law of (1.9) is first order overall.
Even the most complex rate laws can be numerically integrated. Analytical solutions of the rate laws are the integrated rate laws and for the first-order rate law, it follows:

$$\frac{dA}{dt} = -k[A] \rightarrow [A] = [A]_0 e^{-kt} \tag{1.9}$$

where $[A]_0$ is the initial concentration of A at t=0.

For the second-order reaction, there are two types of rate laws, depending on the reaction scheme.

$$\frac{dA}{dt} = -k[A]^2 \rightarrow [A] = \frac{[A]_0}{1 + kt[A]_0} \tag{1.10}$$

$$\frac{dA}{dt} = -k[A][B] \rightarrow \frac{[A]}{[B]} = \frac{[A]_0}{[B]_0} e^{([A]_0 - [B]_0)kt} \tag{1.11}$$

where $[A]_0$ and $[B]_0$ is the initial concentration of A and B at t=0, respectively [7].

5. Electrical resistivity of metals with point defects

Most metals are good electrical conductors, due to the large number of conduction electrons that can be excited into empty states above the Fermi level. The electrical conductivity is a measure of the ease with which a material is capable of conducting an electric current. In fact, the electrical conductivity for the pure Fe at room temperature is $1.0 \cdot 10^7$ $(\Omega \cdot \text{m})^{-1}$, while for Si is $1.0 \cdot 10^3$ $(\Omega \cdot \text{m})^{-1}$. The reciprocal of conductivity is the resistivity, which is the electrical resistance of a conducting material per unit length. Resistivity is a measure of a material's resistance to the passage of electric current and is more easily obtained. Resistance can be calculated, according to Ohm's law, if the applied current is well determined and the voltage is accurately measured, as:

$$R = \frac{V}{I} \tag{1.12}$$

Resistivity ρ is then equal to R times the geometric factor f:

$$f = \frac{S}{l} \tag{1.13}$$

where S and l are the cross-sectional aera and the length of the conductor, respectively. Resistance depends upon the size or the shape of a sample, while the ρ does not. Thus, it a great measure for comparing electrical conductance of various metals or specimens.

Conduction electrons experience collisions (scattering) at various crystalline imperfections which serve also as scattering centers, increasing the resistivity of the metal. The total resistivity of a specimen is the sum of various contributions. These scattering mechanisms act independently of one another and are experimentally observed to arise from thermal atomic vibrations (phonons), which depend on temperature, impurities and point defects in the specimen, which are temperature independent, but depend on the history of the material. These three terms are presented as:

$$\rho(T) = \rho_i + \rho_d + \rho_t(T) \tag{1.14}$$

in which ρ(T) is the resistivity at temperature T and ρ_i the impurity, ρ_d defect and ρ_t phonon contributions, respectively. Equation 1.14 is called Matthiessen's rule [6]. At low temperatures, the thermal contribution, which comes from the vibrations of the crystal and the motion of the lattice, are minimized and as the specimen's temperature reaches the boiling point of liquid helium ($T = 4.2$ K), the ρ_t term becomes negligible. Then, residual resistivity ρ_0 can be determined as:

$$\rho_0 = \rho_i + \rho_d \tag{1.15}$$

In the present work, the residual resistivity after various annealing processes on the specimen is measured at the base temperature of $T = 4$ K. This allows to follow the evolution of the carbon solute atoms and defects.

6. Carbon in steels

Carbon is a main alloying element in steels and can exist in four forms in α-Fe: (1) in interstitial solid solution, (2) as a metastable carbide, called ϵ-carbide, (3) as the Fe_3C carbide ("cementite ") and (4) in the stable form of graphite. Nitrogen and other elements (O,S,P,Cr) are also present in steels, but in minor amounts.

E-carbide is a transition iron carbide with a chemical formula between Fe_2C and Fe_3C. It has a hexagonal closed packed arrangement of iron atoms with carbon atoms located in the octahedral interstices, as shown in Fig. 1.4.

Fe_3C carbide has orthorhombic crystal structure, as shown in Fig. 1.5. All of the cementite appears as small, spherically shaped grains distributed fairly randomly over the iron grains, which have much larger sizes and the typical curved grain boundaries. Cementite is a hard and brittle compound.

All the previously mentioned come from experimental results which are in agreement with theory. On the contrary, even nowadays it is not feasible to locate and identify the specific structures of carbon-vacancy clusters in bcc Fe during thermal processing. Thus, according to literature, the probable C-related defects are: (1) simple interstitial supersaturation, (2) coassociation with vacancies as inferred from reduced vacancy diffusion and carbon segregation to vacancy-rich regions, (3) direct observation of elevated carbon concentration up to 8 at.% near dislocation cores and (4) up to 6.6 at.% at grain boundaries [8]. The formation of a C-vacancy by combing a vacancy with n interstitial carbon atoms can be given schematically, in the form of a chemical reaction as described in Section 4., as:

$$\mathrm{Fe}_V + \mathrm{nC}_i \rightarrow (\mathrm{Fe} + \mathrm{nC}) \tag{1.16}$$

There is also the case of two single vacancies (C-vacancy) clusters forming a divacancy (C-divacancy) cluster, which is schematically presented as:

$$2(\mathrm{Fe}_V + 2\mathrm{C}) \rightarrow (2\mathrm{Fe} + 4\mathrm{C}) \tag{1.17}$$

The phases present in iron-carbon alloys at various temperatures and compositions of iron with up to 6.67% carbon are shown in the Fe-Fe_3C phase diagram of

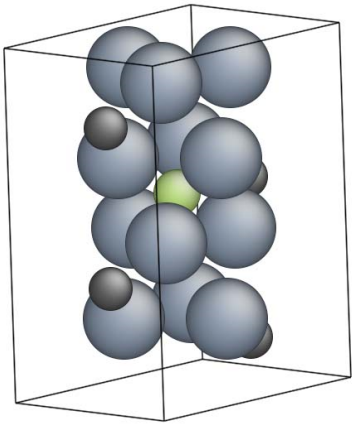

Figure 1.4: E-carbide. Large spheres:iron, small spheres: carbon, light green sphere: carbon position, partially occupied.

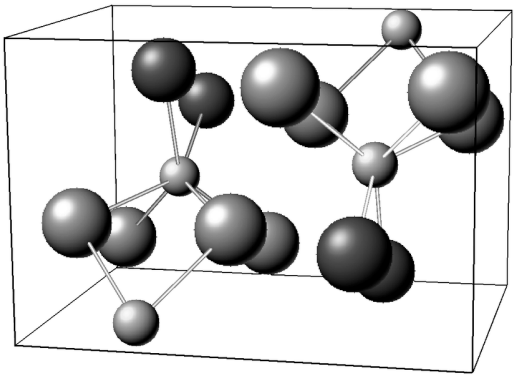

Figure 1.5: Cementite. Small spheres: carbon, dark medium-sized spheres:iron 4c, large spheres: iron 8d positions.

Fig. 1.6.

Carbon atoms are smaller than iron atoms. The atomic radius of the carbon is much less than that of the iron: 0.071 nm versus 0.124 nm. The diameter of carbon atoms is estimated to be 56% of the diameter of iron atoms. Hence, when carbon dissolves interstitially in iron, it pushes the iron atom slightly apart. The more the carbon dissolved, the further the iron atoms are pushed apart. Thus, there is a limit to how much carbon can dissolve in iron. The maximum amount that can be dissolved into ferritic iron in 0.02 wt%, which occurs at the eutectoid temperature of $T = 727°\text{C}$ [9], as illustrated in Fig. 1.7.

Since the solubility of carbon in pure iron is limited, the two carbides can form from the residual carbon impurity content. The transition from ϵ-carbide to cementite appears to occur by nucleation of cementite at the ϵ-carbide/α interfaces, followed by resolution of the metastable ϵ-carbide precipitate [10].

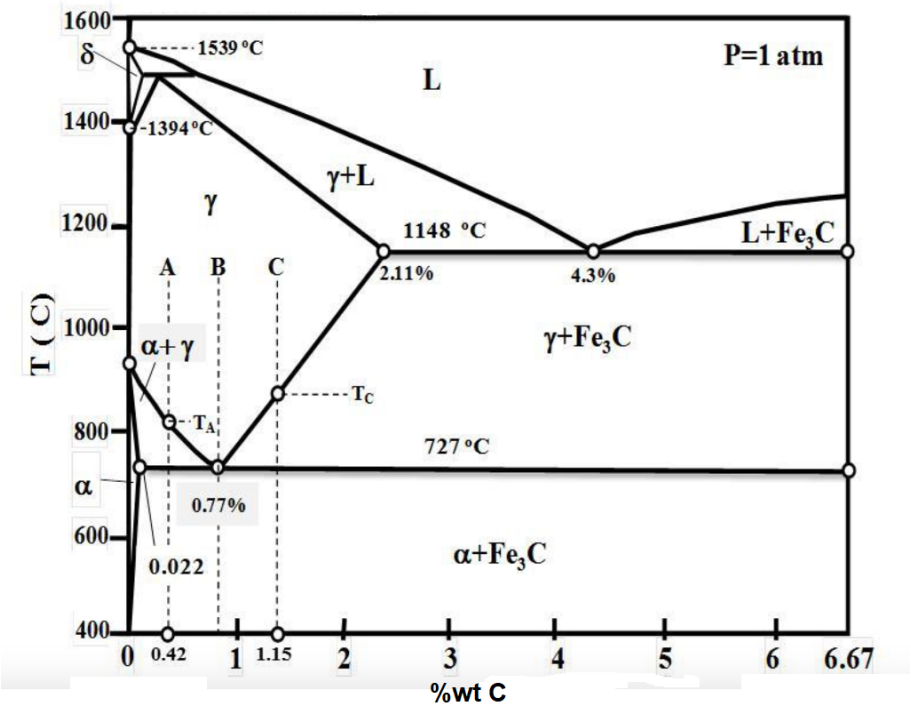

Figure 1.6: The phase diagramm for Fe-Fe_3C system.

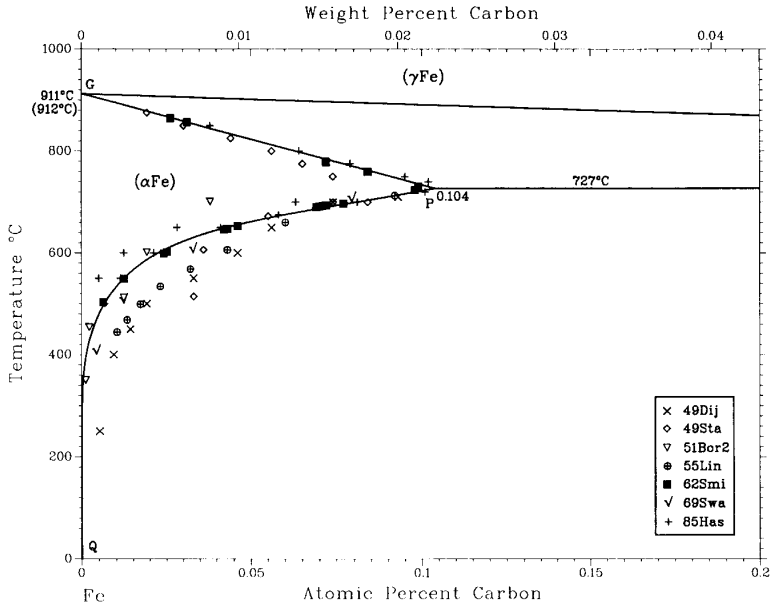

Figure 1.7: α-Fe phase field of the Fe-Fe_3C phase diagram [11].

Chapter 2

Experimental Procedure

1. Sample Preparation

1.1 Starting Materials

The starting materials were high purity alloys obtained from the European Fusion Development Agreement, prepared in Ecole Nationale Superieure des Mines in France under specified conditions. Chemical analysis of the alloys, as well as the residual element analysis was determined by Glow Discharge Mass Spectometry (GDMS). The composition of the alloys is given in Table 2.1.

Alloy	C at. ppm	S at. ppm	O at. ppm	N at. ppm	P at. ppm	Cr ppm/wt
Fe	14	4	7	20	<9	<2 ppm
Fe-C	220	4	4	12	<9	<2 ppm

Table 2.1: Chemical analysis of the alloys.

The purification of iron was obtained by induction melting in a cold crucible, under high purity Hydrogen-Argon atmosphere, in order to eliminate impurities. The Fe-C alloy was prepared the same way but under pure argon atmosphere, to avoid any contamination by impurities. The homogeneity of the alloy is achieved by cutting with a dedicated saw the solidified ingot, mixing the pieces and re-melting. This process is repeated several times. The final preparation stage was for both alloys the same: heat treatment to achieve recrystallisation at $T = 700°C$ for 1 hour

under pure argon flow followed by air cooling. The presence of a second phase was investigated using transmission electron microscope (TEM) observations. For pure Fe there was no other phase observed. On Fe-C, a few small nanoparticles have been observed, which could be carbides with nanometric size and a dislocation density of 5×10^8 cm^{-2}. Table 2.2 contains data obtained from metallurgical studies [12].

Alloy	Lowest Hardness (HV)	Mean Grain Size (μm)	Min and Max Grain Dimensions (μm)
Fe	75	183	4/650
Fe-C	80	265	5/786

Table 2.2: Hardness and grain size of the alloys.

1.2 Specimen Preparation

Starting materials were cylindrical bars of 11 mm diameter. Thin disks (~ 0.5 mm) were cut from the main bar by means of a precision diamond saw. They were cold rolled down to 100 μm thickness. The final stage of samples preparation was electropolishing the foils. It was essential to remove a layer of the surface of the foils, in order to remove impurities and contamination from the previous preparation stages. The foils were electropolished to final thickness of 50μm. The electropolishing solution consists of 50ml phosphoric acid (H_3PO_4) and 25ml sulfuric acid (H_2SO_4). A platinum sheet was used as cathode. The temperature of the solution was stabilized at $T = 85$°C and the voltage at $V = 2.6$ V. The duration of the electropolishing was about t=3 min, depending on the thickness of each foil. Fe-C specimens were cut from the foil in rectangular shape of (18×2) mm by means of scissors. The shape of pure Fe samples was obtained with electrical discharge machining. In particular, they were cut by spark erosion, which was electronically controlled. The shape and dimensions of the samples is given in Figure 2.1.

The samples were subsequently annealed in order to relieve internal stresses created during cold working and dissolve the C solute atoms in the case of Fe-C. Annealing was performed under hydrocarbon-free vacuum of 10^{-6} mbar, so that oxidation and contamination of the samples is prevented. The container of the samples used for the annealing treatment process must be made of aggregate so that it does not react with the samples in the selected temperature range. Therefore, samples are placed in an alumina (Al_2O_3) boat. This is placed in a quartz tube, which is connected to the vacuum pump and positioned in the geometrical centre of the tube furnace for good temperature uniformity. Samples before annealing process

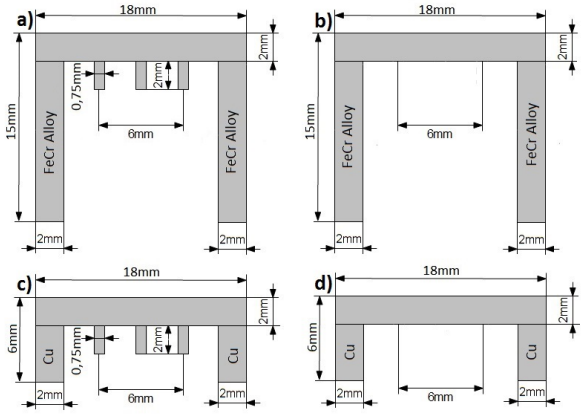

Figure 2.1: Shapes and dimensions of the samples.

are presented in Fig.2.6. Annealing time was $t = 8$ h and the annealing temperature at $T = 730°$C, with heating rate $\Delta T/\Delta t = 5°$C/min. This temperature was selected so as to achieve maximum solubility of C, according to the Fe-C phase diagram (see section 6.).

Additional experiments were carried out, in order to investigate the influence of the annealing temperature and time intervals on the alloys. A number of specimens, prepared by the exact same experimental routine, as to have the same material history with the other specimens, were submitted to an annealing process at lower temperature, specifically at $T = 650°$C, and for significantly smaller time intervals, $t = 1$h.

After annealing the samples were quickly removed from the furnace so that they cool down as fast as possible and avoid C precipitation. The samples were then stored immersed in liquid nitrogen at a temperature of $T = 77$ K until they were used in the experiments. It is noted that the C concentration of the Fe-C alloys (220 appm) is above the solubility limit at room temperature and since C is mobile at $T = 300$ K a slow precipitation process would occur. This was avoided by storing the samples in liquid nitrogen.

Various specimens were examined by an optical microscope at two phases during the sample preparation process, firstly after cold rolling and secondly after annealing. In Fig.2.2, 2.3 one of the pure Fe specimens is presented, while in Fig. 2.4, 2.5 one of the C-doped Fe specimens is shown. In Fig. 2.2 and 2.4, the effects of cold rolling are obvious and the grain boundaries can not be distinguished. In Fig.2.3 and 2.5, the grain boundaries of the crystals after annealing are easily observed on a part of the surface of the specimens. For the pure Fe specimen, the size of the crystals can be estimated, around $\sim 10\mu$ m, whereas for the C-doped Fe spec-

imen, around $\sim 30\mu$ m. Thus, the mean size of the crystals in the pure Fe specimen is apparently smaller than the size of the C-doped Fe specimen.

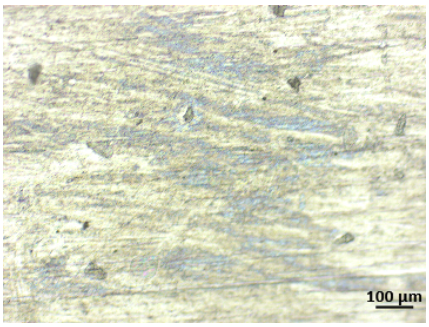

Figure 2.2: Surface microstructure of Fe sample after cold rolling.

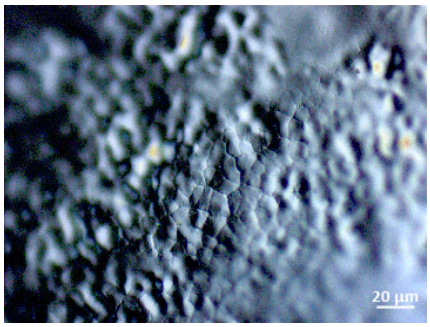

Figure 2.3: Surface microstructure of Fe sample after recrystallization process.

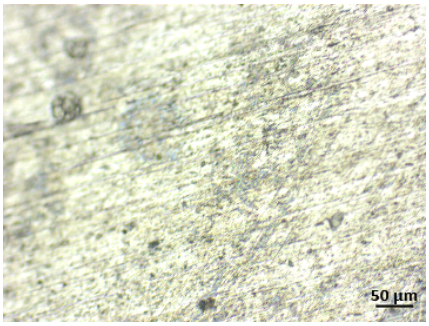

Figure 2.4: Surface microstructure of Fe-C sample after cold rolling.

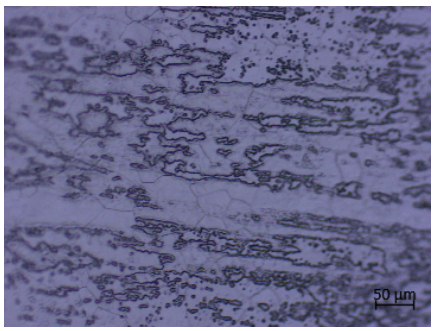

Figure 2.5: Surface microstructure of Fe-C sample after recrystallization process.

1.3 Electrical Contacts on the samples

Electrical resistivity measurements were acquired by standard DC four probe method. High purity (99.5%), 250 µm diameter pure iron wires were used as potential leads. Rectangular strips of FECRALLOY (15×2) mm^2 were used as current/heater leads. The electrical contacts between the samples and the iron leads/FECRALLOY were obtained by resistance spot welding. This process induces "spot "soldering of same or similar materials. Heat generated due to the resistance to the flow of the electric current ($\sim\ 10 - 20$ A) through copper alloy electrodes causes local melting and formation of a continuous solid weld. Pressure is used to help control the contact resistance and the rate of melting at the interface [13]. Samples with electrical contacts are presented in Figure 2.7.

All samples were kept in liquid nitrogen until the measurements were made to avoid precipitation of the C solute atoms.

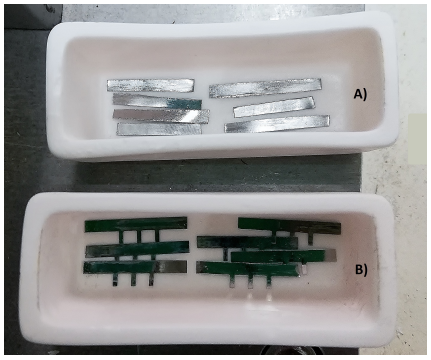

Figure 2.6: Fe-C (A) and pure Fe (B) samples before annealing treatment.

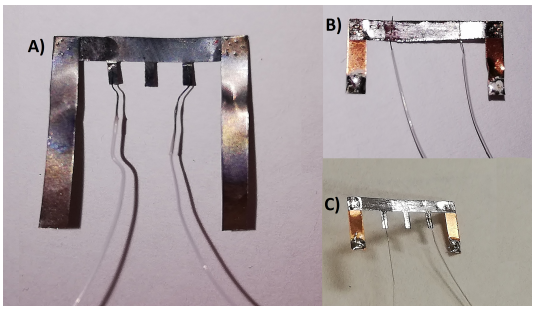

Figure 2.7: (A) Fe, (B) pre-irradiation Fe-C and (C) pre-irradiation Fe samples with electrical contacts, prior to attaching to the sample holder.

2. Experimental Techniques

2.1 Experimental Setup for fast annealing and quenching in liquid He

Residual resistivity measurements is performed in liquid Helium vapor (LHe) shortly after each anneal cycle. Thus, samples must be as distant as possible from the LHe vapor during the annealing interval and immediately quenched in LHe after its finishing. In Fig.2.8, this experimental setup is presented on the left. The sample holder is attached on the edge of a metallic rod (2), inside the LHe dewar, so that the sample is directly above the LHe level. The rod is secured on the upper part of the dewar by an insulating cap made of brass (5), which allows the rod to be moved in the vertical direction, so that the sample is located at the respective distance from the LHe level. This construction isolates the dewar from the surrounding atmosphere, in order to maintain the He in liquid state for as long as possible. The upper part of the rod is sealed with a closing cap made of stainless steel (4), through which the electrical connections are guided from the sample to the lab equipment.

In Fig.2.8, the sample holder (1) is presented on the right. Samples are mechanically attached to the sample holder with a porcelain screw terminal (6), through which the current leads of the sample connect with current leads that are guided outside of the dewar (7). The screw terminal is attached on a perforated metal sheet (9), which is placed at the edge of a metal rod (2), 1.2 m long and 8 mm of diameter,

through which the electrical leads of the samples are guided to the lab instruments. On the back of the metal sheet, there is another screw terminal that connects the samples potential leads to the ones guided out of the dewar (8) [14].

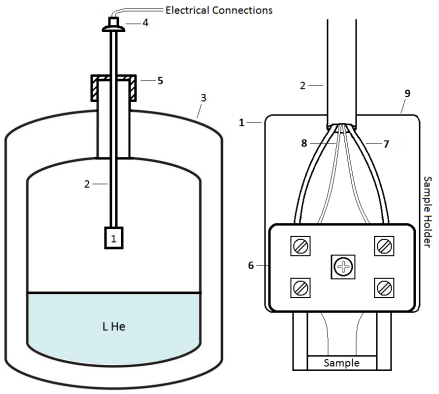

Figure 2.8: Schematic of the annealing experimental setup.

2.2 Electrical resistivity measurements

The electrical residual resistance of the samples is measured by the standard DC 4-probe method, as shown in Fig.2.9. By this technique, the inclusion of the leads and the probes resistance is avoided. A standard reference resistor ($R = 1\ \Omega$) is connected in series with the sample, so that the current flows through both. According to Ohm's law, the current is proportional to the voltage (V_R) as:

$$I = \frac{V_R}{R_R} \tag{2.1}$$

In this case, the sample's resistance is:

$$R_s = \frac{V_s}{I} = \frac{V_s}{V_R} R_R \tag{2.2}$$

with V_s the voltage drop at sample's edges.

The resistance measurements are performed at $T = 4$ K, while the measuring instruments and the wiring are at room temperature. So temperature gradients appear, which generate thermoelectrical voltage due to Seebeck effect. Thus, the measured voltage (V) is the sum of the thermal voltage (V_{th}) and the voltage drop at sample's edges (V_s):

$$V = V_{th} + V_s. \tag{2.3}$$

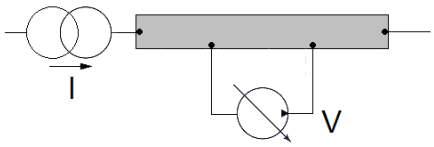

Figure 2.9: Schematic of the four probe method.

Supposing that the thermoelectrically generated voltage does not change polarity and by using a bipolar current source, the resistance is measured as:

$$\frac{V_+ + V_-}{2|I|} = \frac{(V_s + V_{th}) - (-V_s + V_{th})}{2|I|} = \frac{V_s}{|I|} = R_s \tag{2.4}$$

with V_+/V_- the measured voltage of the sample, depending on the polarity of the DC current.

For this accurate resistance measurement the current is supplied by a dual output DC power supply Agilent (E3646A), 0-8V/3A or 0-20V/1.5A and the voltage measurements of high accuracy are made by a digital nano-voltmeter (Keithley 2182A NANOVOLTMETER). The measurement is computer controlled and the absolute error of each resistance measurement is calculated automatically within the control program, each time taking into account the individual errors of the measured voltage and applied current. All factors considered, the absolute error of the experimental setup was in the range $\sim 0.1 - 1\mu\Omega$.

The annealing of the samples is achieved by ohmic self-heating of the FECRALLOY strips and the sample itself. The power supply used for this part of the experiment is a Dual 60V/20A 420W DC Power Supply (TTi CPX400DP). After each anneal cycle, the sample is rapidly quenched and the resistance is measured. In Fig.2.10, the electrical circuit of the annealing experiment setup is presented. Two different electrical loops are used: the first one during the annealing of the sample and the second during the resistance measurement. The use of several switches regulates the use of each loop.

2.3 Automatic control of the resistance/temperature of the sample

The stability of the temperature of the sample and the current flow during the annealing interval are monitored with a control program. In this particular experimental setup, the intended resistance of the sample and the time interval of the annealing are the inputs for the specific-designed routine. This routine calculates the current

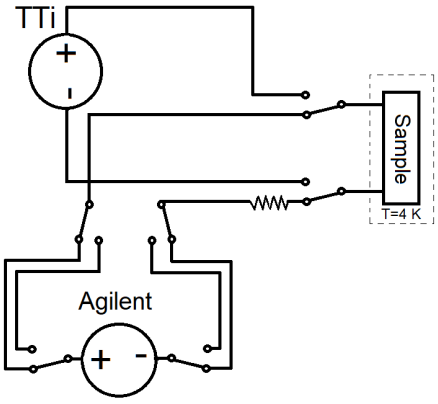

Figure 2.10: Schematic of the electrical connections, presenting two different loops used in turns in this experimental setup. Loop including Agilent power supply is used for the resistance measurements of the specimen. Loop including TTi power supply is used for the ohmic self-heating of the specimen.

that needs to be given by the power supply for the sample to have the intended resistance. At first, a small current flow is applied and at regular intervals the sample's resistance is calculated from the measured voltage and the current flowing at that moment. The sample's voltage is measured with a digital multimeter connected to the computer. The possible difference found between the measured and the intended resistance imposes the routine to change the current flow from the power supply to a better-fitting value.

In order to maintain stability and get better feedback from the annealing system, a Proportional-Integral (PI) controller was included, which is a special case of the Proportional-Integral-Derivative (PID) controller. This is a control loop feedback mechanism, in which the derivative of the error is not used. The main task of this controller is to continuously calculate the difference between the setpoint (SP) and the measured variable (MV) and to apply a correction based on proportional and integral terms. The controller output is given:

$$u\left(t\right) = k_p \cdot e\left(t\right) + \frac{k_p}{T_i} \cdot \int_0^t e\left(\tau\right) d\tau \tag{2.5}$$

where k_p is the proportional gain, $\frac{k_p}{T_i}$ is the integral gain, T_i is the integral time constant and $e\left(\tau\right)$ is the error or deviation of actual measured value (PV) from the setpoint. The proportional gain and the integral time constant are tuning parameters associated with the power and the time provided, in order to achieve the intended value. The optimum values for these parameters can minimize the overshoot of the setpoint, the oscillations of the system and the time needed to reach the setpoint.

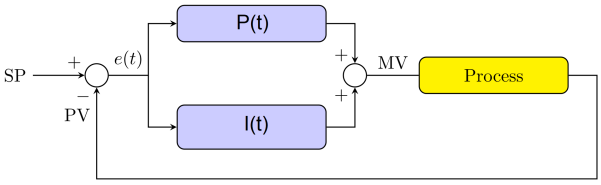

Figure 2.11: Basic block of a PI controller.

The optimal values of k_p and T_i were determined with the Ziegler-Nichols method [15]. This method depends on the calculation of the ultimate gain k_c, at which the output of the control loop has stable and consistent oscillations, and the oscillation period T_c. According to Ziegler-Nichols method, the optimum settings for a PI controller are determined as:

$$k_p = 0.4k_c, T_i = 0.8T_c.$$

For the experimental setup, the optimum values for these tuning parameters were:

$$k_p = 3.2, T_i = 1.2.$$

2.4 Tandem Accelerator

Samples irradiation was performed at the TANDEM accelerator of NCSR "Demokritos"
with 5MeV protons. As presented in Fig.2.12, this accelerator is an electrostatic Van de Graaff Tandem accelerator with a maximum acceleration voltage of 5 MV. Negative ions are formed from an ion source (I) at ground potential and are accelerated to the positive high-voltage terminal. The charging belt (B) is made of insulating material and it passes over two rollers, one motor-driven at ground potential and the other in the high-voltage terminal, well insulated from ground. Charge is sprayed onto the moving belt from sharp corona, is conveyed to the high-voltage terminal and is removed by collector points on the surface of the electrode, where it is allowed to flow [16]. The formed ions, entering the high-voltage terminal, are deposited on the belt and in a stripper (S) system lose a few electrons and change charge into positive ions. The stripper system is usually a thin carbon foil. Through this second stage, they gain energy once more.

The energy of the ion beam depends on the electric charge q of the positive charged ions and equals: $E = (q + e)V$, where V is the terminal voltage, e is the elementary and q is the charged state of the ion, which is equivalent or multiple of e, depending on the ion. Thus, in case of protons and deuterium: $E = 2V$.

The beam line operates under high vacuum ($\sim 10^{-6}$ mbar), achieved by vacuum pumps, which exist in various spots along the line. The diffusion of the beam is fully monitored before the irradiation of the samples. In particular, the beam falls on a thin aluminum lamella, which works as a scatterer and forms the diameter to D $\sim 20 - 40$ mm. The scatterer is located about 2.5 m away from the samples. Thus, the beam falls on the sample uniformly, without any deviations in its intensity. The cross section of the beam is determined by a slit, which can be shaped from four movable metallic sheets [17].

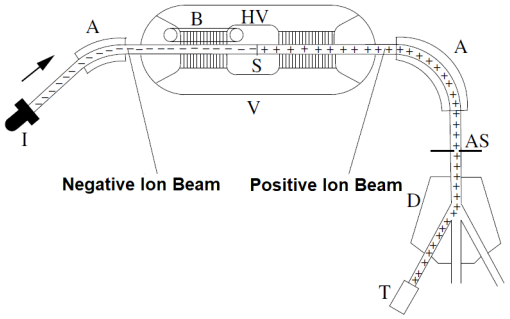

Figure 2.12: Schematic of the Tandem Accelerator. I: Negative ion source, V: Vessel under high pressure, B: Charging belt, HV: High voltage terminal, S: Stripper, A: Analyzing magnet, AS: Velocity selector, D: Switching magnet, T: Target.

2.5 Ion Irradiation Facility

Irradiation of the samples was performed in the dedicated materials irradiation facility IR^2, which is coupled to the accelerator beam line. The setup of this facility keeps the samples at the cryogenic temperature during irradiation by means of a closed-cycle He refrigerator. The setup also allows the simultaneous real-time monitoring of radiation damage via in-situ measurement of electrical resistivity of the samples. Furthermore, it permits the fast heating/cooling of the samples from cryogenic (≤ 5 K) to high temperatures (≥ 350 K). The sample holder is made of Al and is placed at the second stage of the cryostat, which is kept at about $T = 4$ K during the whole process. It could carry 6 samples, which could be annealed all together in an identical program. It also provides the ability for samples to be irradiated in couples simultaneously, separately from the others. In this way it is possible to irradiate groups of two samples (pure and C-doped Fe) together to three different irradiation doses. The sample holder is surrounded by metal heat shields, which prevent the heat transfer through radiation from the surrounding environment in the facility, which is at room temperature. The heat shields are in thermal contact with the cryostat, at $T = 50$ K.

On the surface of the sample holder, an insulating thin sheet made of mice is attached, in order to secure the electrical insulation of the sample, but to allow thermal conductivity. Samples are secured on the sample holder with GE varnish, after all electrical connections are checked.

3. Measurement programme

3.1 Annealing of Un-irradiated Samples

After recrystallization process, all samples were annealed according to a conventional isochronal program mentioned in the literature. The annealing temperature was increased keeping a constant ratio of $\Delta T/T \approx 0.03$ from $T = 300$ K up to 700 K. The annealing time intervals were isochronal ($\Delta t = 300$ s). At the end of each interval, the sample was rapidly quenched in LHe ($T = 4$ K) and the residual resistivity was measured. Thus, the variation of residual resistivity was obtained as a function of annealing temperature.

The codification of the samples emerge from the numbers of the stripes they were cut from. There were five different samples stripes prepared, following the same experimental procedure, Fe-C 31,32,34,35, and 36. For example, Fe-C 31 and 31(2) are two samples cut from the same stripe before the recrystallization process, but submitted to it simultaneously.

In order to convert the measured resistance (in Ω) to absolute resistivity (Ω-cm), the sample geometric factor had to be calculated. This calculation involves the sample's resistance at $T = 273$ K and the resistivity of pure Fe, $\rho_{273K} = 8570$ nΩ-cm as found in the literature [18]. So, the geometric factor f was obtained by the following relation:

$$f = \frac{\rho_{273K}}{R_{273K} - R_{4K}} \tag{2.6}$$

where R_{273K} and R_{4K} is the measured sample resistance in ice-water solution and in LHe, respectively.

All samples, before the annealing process, were submitted to resistance measurements immersed in ice-water bath (273 K), in liquid nitrogen (77 K) and in liquid helium (4 K). The resistance was measured by applying an electrical current, measuring the resulting voltage and applying Ohm's law. The measuring current applied at each temperature was: ($I = 0.01$ A, $T = 300$ K), ($I = 0.02$ A, $T = 273$ K),

Sample	R_{300K} (mΩ)	R_{273K} (mΩ)	R_{77K} (mΩ)	R_{4K} (mΩ)
pure Fe	6.902(2)	5.780(5)	0.4260(2)	0.0435(4)
Fe-C, 31	5.747(6)	5.079(5)	0.4145(3)	0.0861(4)
Fe-C, 31(2)	6.164(5)	5.371(6)	0.4755(2)	0.1219(4)
Fe-C, 34	5.972(7)	5.232(4)	0.4527(1)	0.1077(4)
Fe-C, 35(2)	5.883(2)	5.209(1)	0.4159(2)	0.0796(1)
Fe-C, 36	6.209(2)	5.453(1)	0.4448(1)	0.0918(3)

Table 2.3: Resistance measurements for un-irradiated Fe and Fe-220 ppm C samples.

($I = 0.05$ A, $T = 77$ K), ($I = 0.5$ A, $T = 4$ K). The resistance and corresponding resistivity values obtained from these measurements and calculations are presented in Tables 2.3 and 2.4.

The concentration of carbon in the C doped samples could be estimated by the following relation:

$$C = \frac{\rho_{sample} - \rho_{Fe}}{\rho_C} \tag{2.7}$$

where ρ_{Fe} and ρ_{sample} are the resistivity of the pure and the C-doped iron sample at given temperature, respectively, and ρ_C is the specific resistivity contribution of carbon atoms in nΩ-cm/ppm. The calculation was applied to the resistivity of Fe-C specimens measured at $T = 4$ and 77 K, where $\rho_C = 0.49$ and 0.6 nΩ-cm/ppm, respectively [19]. The results are given in Table 2.4. The fact that the C concentration estimated from the 4 K resistivity appears larger is indicating that the interstitial defects determine the residual resistivity, since the thermal contribution is vanished, according to Matthiessen rule.

Sample	ρ_{273K} (nΩ·cm)	ρ_{77K} (nΩ·cm)	ρ_{4K} (nΩ·cm)	f (nΩ·cm)	C_{77K} at. ppm	C_{4K} at. ppm
pure Fe	8634(10)	636(1)	65(1)	1494(1)		
Fe-C, 31	8717(10)	710(2)	147(2)	1716(2)	124	169
Fe-C, 31(2)	8769(10)	776(2)	199(2)	1632(2)	233	274
Fe-C, 34	8750(7)	757(1)	180(1)	1672(1)	201	235
Fe-C, 35(2)	8702(2)	695(1)	133(1)	1671(1)	98	139
Fe-C, 36	8716(2)	711(1)	147(1)	1598(1)	124	167

Table 2.4: Sample data for un-irradiated Fe and Fe-220 ppm C alloy.

3.2 Annealing of Irradiated Samples

Irradiation of Fe and Fe-220 ppm C specimens was performed at the TANDEM accelerator of NCSR Demokritos with protons of energy 5 MeV and flux $9 \cdot 10^{11}$ cm^{-2} s^{-1}. Three pairs of samples were irradiated at three different doses, as presented in Table 2.5. Each pair, consisting of one pure and one C-doped Fe sample, was irradiated simultaneously. The temperature of the samples during irradiation was approximately $T = 25$ K. The proton beam creates point defects inside the material due to atomic displacements after collisions of the energetic protons with the nuclei. These defects are mainly self-interstitial atoms and vacancies (Frenkel pairs - FP). The residual resistivity of the specimens increases due to the present of the defects. The total resistivity increase in each specimen is given in Table 2.5. As seen from the data, the resistivity increase is almost the same (within $\pm 5\%$) in specimens of the same pair. Using the value of the specific resistivity per FP $\rho_F = 3.0$ nΩ-cm/ppm [20] we obtain an estimate of the FP concentration in the specimens, which is also given in the table.

After irradiation the samples were annealed up to 300 K in the irradiation chamber and then taken out and stored in liquid nitrogen. Then they were taken one-by-one and isochronically annealed in the experimental setup described in section 2.1 according to the same program followed in the case of un-irradiated samples: annealing interval $\Delta t = 300$ s, temperature step $\Delta T/T = 0.03$, range $300 < T < 700$ K.

Dose	Total Dose (cm^{-2})	Alloy	Total Resistivity Increase (nΩ-cm)	Defect conc. (ppm)
Low	$0.5 \cdot 10^{16}$	Fe	100	33
		Fe-C	98.2	33
Medium	$1.8 \cdot 10^{16}$	Fe	319	106
		Fe-C	306.2	102
High	$4.5 \cdot 10^{16}$	Fe	813.2	270
		Fe-C	792.3	264

Table 2.5: Sample data for 5MeV proton irradiated Fe and Fe-220 ppm C alloy.

Chapter 3

Experimental results

1. Isochronal Annealing of un-irradiated pure and C-doped Fe

Isochronal annealing was performed in pure and C-doped Fe specimens in the temperature range $300 < T < 700$ K. The annealing temperature was increased in steps ΔT, keeping a constant ratio $\Delta T/T \sim 0.03$. The holding time at each temperature was $\Delta t = 300$ s. The samples were brought to the annealing temperature by means of ohmic self-heating and then quenched in LHe vapor, as described in Chapter 2, section 2.1. The residual electrical resistivity was measured at LHe temperature after each annealing step.

Several specimens were measured, in order to check the reproducibility of the procedure. From the measurement curves that came out, it appeared that the Fe-C samples can be divided in two different categories, based on the initial value of the electrical resistivity after the homogenization annealing. Representative samples from the two categories are discussed here.

Figure 3.1a shows the variation of the residual resistivity as a function of annealing temperature in pure Fe and in Fe-C samples that exhibit initially a relatively high residual resistivity after homogenization, $\rho \gtrsim 180$ nΩ-cm. This type of annealing curve is also frequently termed "resistivity recovery", when it refers to the recovery of defects in the material, which have been previously generated by, e.g., deformation or irradiation. In the present case the term "recovery" will be used by analogy, although there is no real defect recovery. From the figure it seen that the resistivity of pure Fe remains unchanged up to an annealing temperature of ~ 600

Sample	Initial (nΩ·cm)	Final (nΩ·cm)	Resistivity Drop (nΩ·cm)	Fractional change %
pure Fe	65.4	68.7	-3.3	-4.5
Fe-C, 31(2)	199.0	106.1	93.0	46.7
Fe-C, 34	180.5	101.7	78.8	43.7
Fe-C, 35(2)	133.1	113.2	19.8	14.9
Fe-C, 31	147.4	111.4	36.0	24.4
Fe-C, 36	146.7	114.1	32.7	22.3

Table 3.1: Resistivity data for un-irradiated pure and C-doped Fe alloys.

K. Above this temperature a slight rise in the resistivity could be observed, which was attributed to possible oxidation of the sample at $T > 600$ K. During oxidation, Fe atoms at the sample surface interact with O to form a thin oxide layer. This effectively reduces the overall thickness of the sample, which is perceived as an increase in resistivity. Due to this oxidation effect, only results for annealing up to 600 K will be considered for both Fe and Fe-C samples.

The resistivity of Fe-C samples, as seen in fig. 3.1a, decreases gradually with increasing annealing temperature and reaches a minimum value of 105 to 110 nΩ-cm after annealing at 580 K. The resistivity then increases again as the temperature rises above 600 K. Two distinct stages can be observed in the course of the resistivity decrease, which are designated as "Stage A" and "Stage B". The stages are more clearly distinguished if we plot the rate of resistivity variation with respect to annealing temperature, $d\rho/dT$. This is shown in fig. 3.1b, where the derivative $d\rho/dT$ is calculated numerically simply by taking differences of consecutive experimental points. The two stages A & B appear as peaks in this figure, centred at $T_A = 440$ K and $T_B = 540$ K, respectively.

Fe-C samples belonging to the second category with a lower initial resistivity $\rho \lesssim 150$ nΩ-cm exhibit a slightly different behaviour upon annealing as can be seen in figures 3.2a and 3.2b. The reduction of residual resistivity again proceeds in two stages, however, stage A is significantly lower in amplitude in this case. Furthermore, the centre of stage A shifts to lower temperature $T_A = 400$ K while stage B appears at roughly the same temperature as in the other sample category. The final resistivity of the samples after annealing at 600 K is again 110 nΩ-cm.

The initial and final resistivity values for all samples are reported in Table 3.1. The total fractional resistivity variation is $\sim 45\%$ in the samples with high initial resistivity and 15-25 % in the those with low initial resistivity.

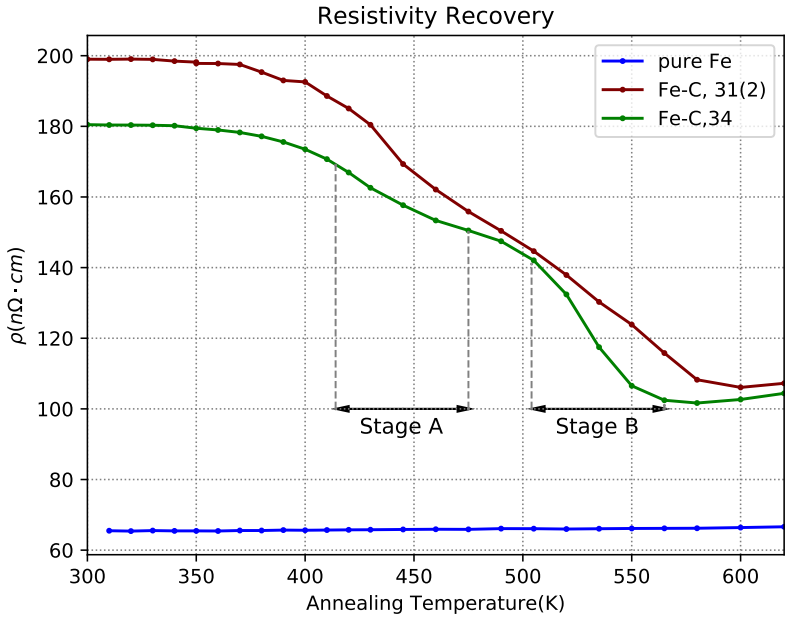

(a)

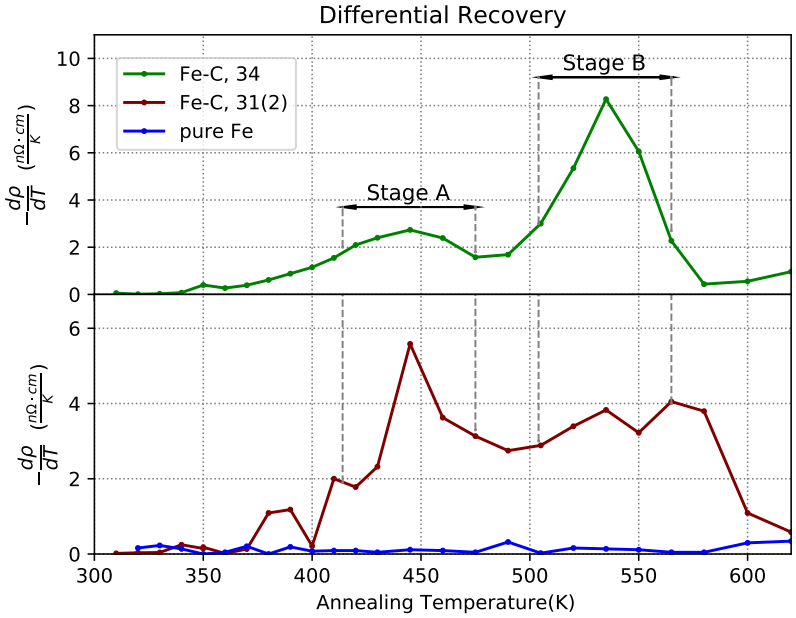

(b)

Figure 3.1: Typical variation as a function of annealing temperature T of (a) the electrical resistivity ρ (also termed "resistivity recovery") and (b) the corresponding change rate $d\rho/dT$ for Fe and Fe-C samples with high initial resistivity, $\rho \gtrsim 180$ nΩ-cm.

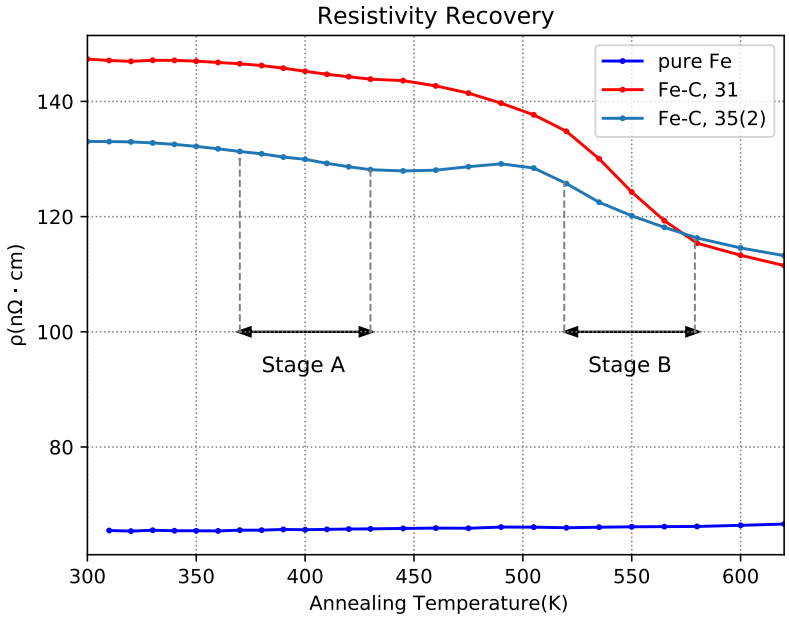

(a)

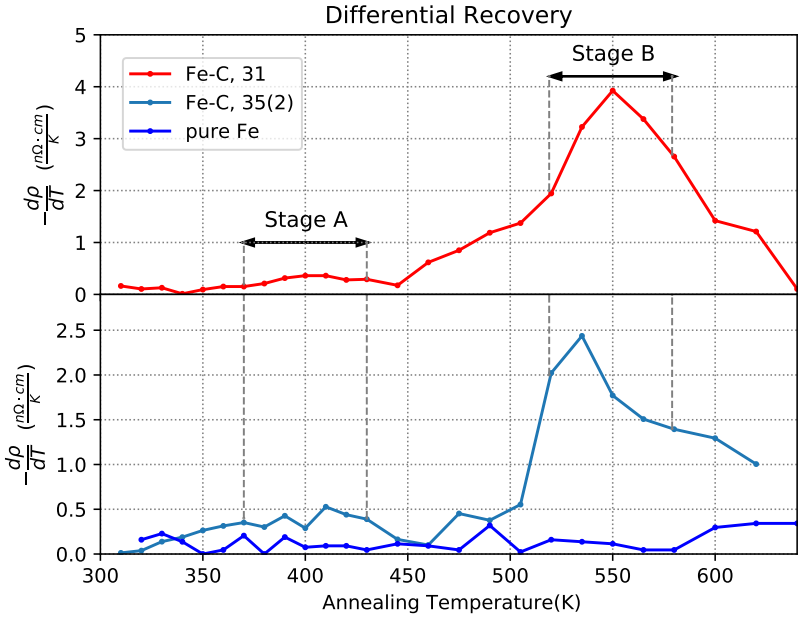

(b)

Figure 3.2: Typical variation as a function of annealing temperature T (a) of the electrical resistivity ρ (also termed "resistivity recovery") and (b) of the corresponding change rate $d\rho/dT$ for Fe-C samples with lower initial resistivity, $\rho(300\ \mathrm{K}) \lesssim 150$ nΩ-cm. Results for pure Fe also shown for comparison

1.1 Discussion

The observed variability in the value of the initial resistivity of the Fe-C samples is attributed to different final concentration of C atoms in solid solution, which depends sensitively on the sample preparation conditions and particularly on the solution treatment at 730°C. To exclude the possibility that C is extracted from the sample during the high temperature annealing, e.g., by some reaction of C with residual gas atoms in the vacuum chamber, we tested a lower solution treatment temperature of 650°C. According to the phase diagram the nominal amount of C is still soluble in α-Fe at this temperature. However, the sample annealed at 650°C showed similar results of resistivity annealing. Further, we tried reducing the total annealing time from 8 hours down to 1 hour also with no difference in the final results. Thus, the sample preparation phase which is most probably responsible for the different final C concentration among samples is the cooling just after solution treatment. Since the samples where cooled in room temperature, without any special provision for, e.g., quenching in water or other liquid, it is expected that the level of C precipitation that may occur during the cooling from high temperature may vary from run to run. The sensitivity of Fe-C resistivity on preparation conditions has been previously reported also by other authors [21].

From the value of initial resistivity of Fe-C samples an estimation of the C concentration in solid solution is possible as shown in Chapter 2, section 3.1. In the samples having high initial resistivity $\rho \gtrsim 180$ nΩ-cm the estimated C concentration is found in the range 200-230 ppm, which agrees with the nominal C content of the starting material. Thus, for these samples we can assume that all of the C remains dissolved in the matrix after solution treatment. On the other hand, in samples with lower initial resistivity, some of the C has precipitated most probably during the cooling phase. The amount of C in solid solution in this case is in the range 100-125 ppm, i.e., 50% of C atoms have precipitated.

The stages A and B observed in the resistivity annealing curves of Fe-C specimens are due to carbon precipitation kinetics and have been previously observed in similar alloys [21, 22]. According to previous authors [22] and recent theoretical calculations [23], stage A corresponds to the initial precipitation of carbon into the metastable ε-carbide phase [10], which has a higher nucleation rate at lower temperatures [23]. Stage B is associated with the precipitation of the stable cementite (Fe_3C) phase. The observed drop in electrical resistivity associated with precipitation is due to the fact that the resistivity per C atom is higher when C is in solid solution in the matrix than when it is part of a precipitate. From the data of Table 3.1, assuming that all C atoms have precipitated at the end of the isochronal annealing, we can estimate that resistivity per C atom in precipitates is 1/3 of the resistivity of C in solid solution.

The observed suppression of stage A in the samples that exhibit lower initial resistivity, $\rho \lesssim 150$ nΩ-cm, indicates that in these samples the precipitation of metastable ε-carbide has probably occurred already during their cooling from the solution treatment temperature.

2. Post-Irradiation Isochronal Annealing in pure and C-doped Fe alloy

The pure and C-doped Fe samples irradiated by 5 MeV protons at cryogenic temperature ($T = 25$ K) were isochronically annealed, initially in the irradiation chamber up to 300 K and subsequently in the experimental setup described in Chapter 2, section 2.1 for temperatures $300 < T < 700$ K. The 2nd annealing program was exactly the same as for the un-irradiated specimens described in the previous section. The evolution of the electrical resistivity of the samples as a function of annealing temperature is shown in fig. 3.3a. Here, the fraction $\Delta\rho/\Delta\rho_0$ is plotted, where $\Delta\rho_0$ denotes the total resistivity increase due to low-temperature irradiation (Chapter 2, Table 2.5) and $\Delta\rho$ denotes the remaining resistivity increase after each annealing step. Results are displayed for the three irradiation dose levels: low, medium and high. As seen in the figure, in pure Fe a fraction around 5-7% of the initial resistivity increase is still retained after annealing at 300 K. The corresponding fraction in Fe-C is higher, around 8-11%. At about 330 K the resistivity of irradiated Fe-C alloys exhibits a sharp drop and becomes very nearly equal to the resistivity of irradiated pure Fe. This drop in resistivity is called a "recovery stage" and is denoted stage IV_A. In the differential resistivity recovery shown in fig. 3.3b, the stage is seen as a sharp peak at 330 K in all irradiation doses.

Above stage IV_A, the resistivity of both Fe and Fe-C reduces slowly until at about $T = 500 - 550$ K the irradiated Fe-C specimens exhibit a 2nd large drop in resitivity, whereupon $\Delta\rho$ becomes negative, i.e., the resistivity after annealing becomes lower than its pre-irradiation value. This effect is more pronounced in the low dose curve. The second drop in resistivity is called stage IV_B and occurs at 550 K after low dose irradiation and at 580-600 K in the medium and high irradiation doses, as seen in fig. 3.3b.

The irradiation-induced resistivity increase in the high and medium dose pure Fe samples anneals out completely at around $T = 600$ K. The resistivity returns to the pre-irradiation value (reaches zero), which is indicated by the dotted horizontal line. Thus, it is assumed that, at this temperature range irradiation defects have vanished and all irradiation damage is eliminated.

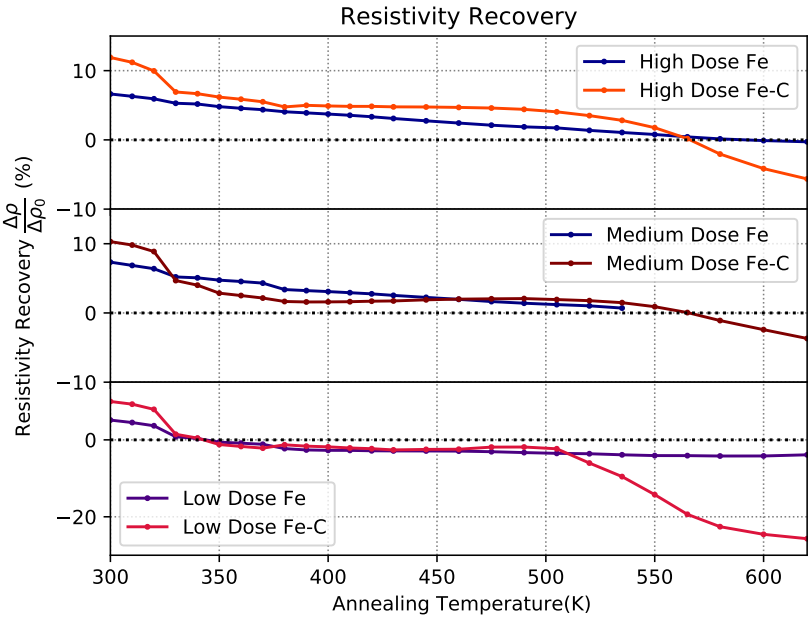

(a)

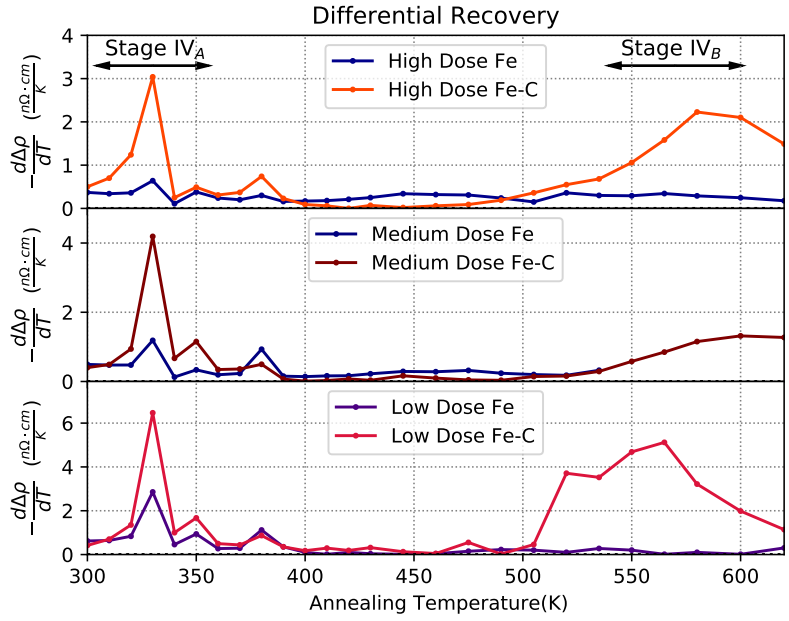

(b)

Figure 3.3: (a) Resistivity recovery and (b) recovery rate as a function of annealing temperature for Fe and Fe-C samples after proton irradiation at T=25 K

2.1 Discussion

The observed resistivity recovery in the proton irradiated pure and C-doped iron can be interpreted as follows. After annealing at 300 K the C-doped samples exhibit a higher fraction of retained irradiation induced resistivity with respect to pure Fe. This indicates that the presence of C inhibits the recovery of some irradiation defects. This could be effected by trapping of otherwise mobile defects in an immobile cluster formed in association with carbon. A possible candidate for this process is the vacancy defect, which is known to interact favourably with C towards formation of vacancy-C clusters (VC). The clusters form at lower temperature (~ 250 K) where vacancies in Fe are mobile [24]. At 340 K where stage IV_A occurs, the VC clusters become mobile and interact with other defects whereupon the vacancy is annihilated. This gives rise to the resistivity drop in stage IV_A.

The higher temperature stage IV_B is associated with carbon precipitation in Fe-C alloys. This is shown by the fact that at this stage the resistivity goes below the pre-irradiation value, just as in un-irradiated specimens the resistivity drops due to carbon precipitation. The effect of irradiation on the process of carbon precipitation will be discussed in detail in the next section.

3. Comparing resistivity recovery rate in irradiated and un-irradiated pure and C-doped Fe alloys

The differential recovery curves of un-irradiated and irradiated specimens are plotted together for comparison in Fig. 3.4 and 3.5. In the upper subplot the un-irradiated specimens are presented, while on the lower subplot the irradiated ones. As previously mentioned, samples can be classified according to their quenched resistivity. So, in Fig. 3.7, the high-quenched resistivity specimens are chosen to be compared, while in Fig. 3.8, the low-quenched ones. The high-dose Fe-C quenched resistivity was high, similar with the C-34 and the C-31(2), in contrast to the medium- and low-dose Fe-C, which was low and comparable to the C-31 and C-35(2).

In Fig. 3.7, where the high-quenched resistivity samples are displayed, it is quite clear that different stages appear in the samples, whether irradiated or not. At low temperature region of this figure, the most noticeable difference is the presence of stage IV_A around $T = 330$ K in the irradiated samples, as well as the its absence from the un-irradiated ones. The opposite occurs for stage A, which is recorded

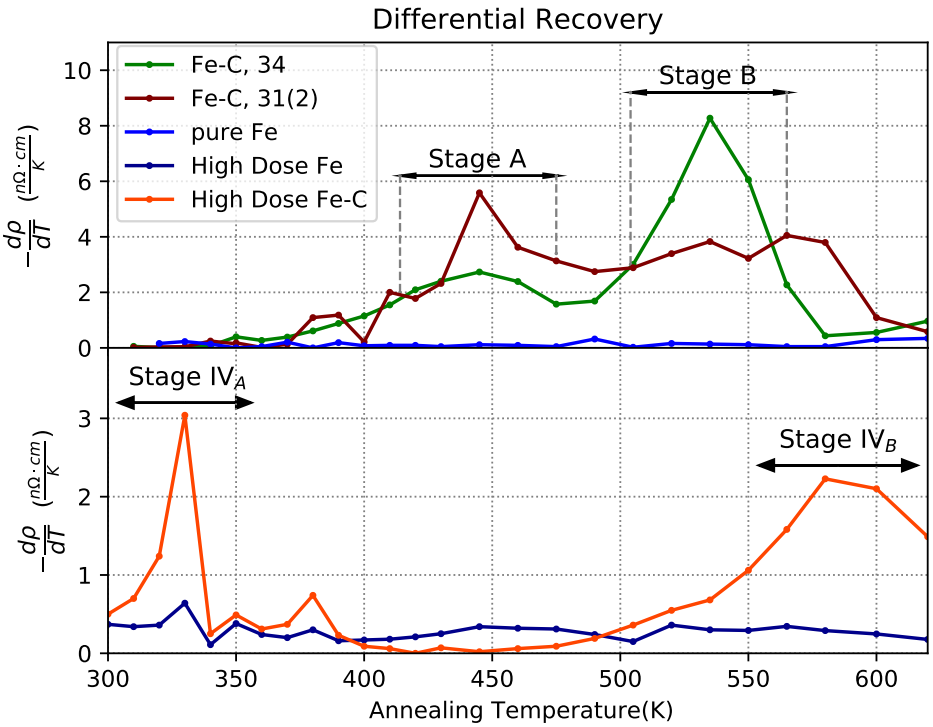

Figure 3.4: Differential resistivity recovery as a function of annealing temperature for high-quenched resistivity Fe and Fe-C samples.

only in the un-irradiated specimens around $T = 445$ K. Stage B and IV$_B$ appear in both cases, at $T = 535$ K and $T = 585$ K, respectively. For the irradiated samples, it is shifted to higher temperature, approximately $\Delta T = 50$ K. It is concluded that these peaks have the same origin, since they are recorded in the same temperature range.

In Fig. 3.8, where the low-quenched resistivity samples are displayed, the recording of the peaks is similar to the ones in Fig. 3.7. Stage IV$_A$ appears around $T = 330$ K in the irradiated samples. Stage A appears around $T = 400$ K in the un-irradiated ones. Stage B and IV$_B$ appear in both cases centered at $T = 550$ K, indicating the same origin.

All things considered, stage IV$_A$ appears only in irradiated specimens and is much larger in Fe-C alloy. Thus, there has to be a connection with irradiation produced defects, which do not exist in un-irradiated specimens. Carbon atoms are mobile in this temperature region and are trapped by irradiation defects. This leads to formation of defect complexes, such as Vacancy-C, which lower the resistivity

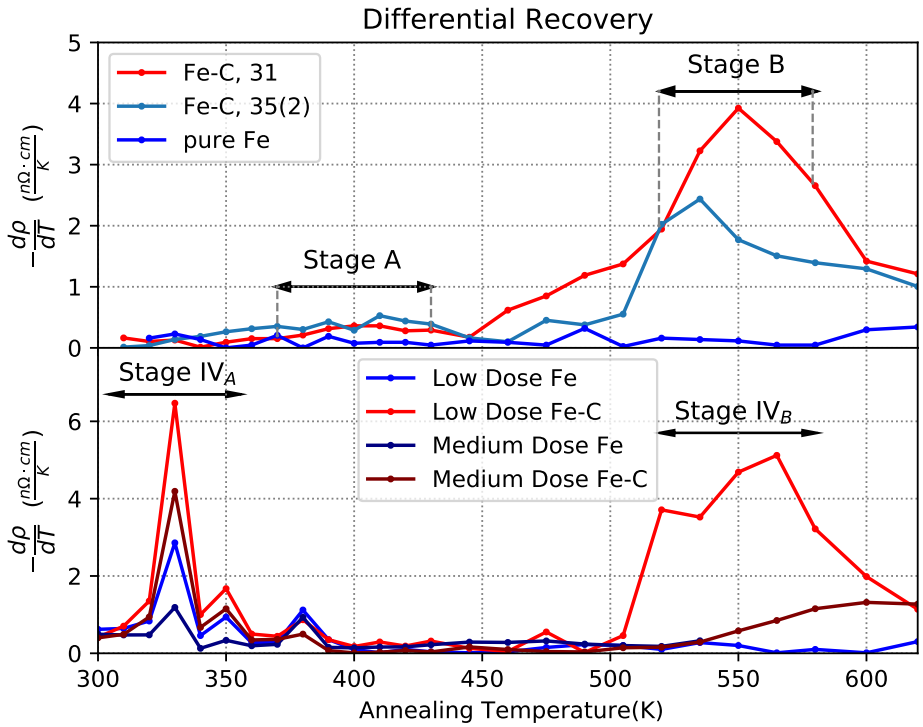

Figure 3.5: Differential resistivity recovery as a function of annealing temperature for low-quenched resistivity Fe and Fe-C samples.

of the sample. Hence, this drop in resistivity, as reflected in stage IV$_A$, can be attributed to carbon migration and clustering. In the pure Fe alloy, the residual C concentration, which is around 20 ppm, induces the appearance of this stage. This is quite clear as the total area of the Fe alloy is about half that of the Fe-C alloy.

Stage A appears only in un-irradiated Fe-C samples and is attributed to the initial precipitation of carbon in a metastable phase. Excess carbon precipitates on dislocations and in the matrix and a phase referred to as ϵ-carbide ($Fe_{2.4}C$) appears.

The difference between the Stages B and IV$_B$ are located in the same temperature region. This points out the fact that these two stages must have the same origin. According to literature, in this temperature range, the formation of Fe_3C occurs without any evidence that this phenomenon is connected with the prior formation of the metastable carbide. The formation of this carbide leads to the drop of resistivity, hence the appearance of the peak/stage in the differential curve. Stage B in case of the high-quenched specimens appears at lower temperature in the un-irradiated and shifted in the irradiated ones. Irradiation defects seem to retard the

carbide formation in the high-quenched resistivity samples. For the low-quenched, this stage appears centered ($T = 550$ K). This depicts that irradiation defects does not affect the carbide formation for the low-quenched resistivity samples.

Chapter 4

Conclusions

- We measured the resistivity recovery of un-irradiated and proton irradiated pure Fe and Fe-C alloys during isochronal annealing in the range $300 < T < 700$ K.
- No change was detected in the resistivity of un-irradiated pure Fe during the annealing process.
- In the un-irradiated Fe-C alloy the resistivity drops during annealing in two distinct stages: A at 440 K and B at 540 K. These stages have been previously observed and are associated with the precipitation of metastable ε-carbide and stable cementite, respectively.
- In pure Fe irradiated by protons at low temperature (25 K), a fraction of about 5-7% of the total radiation induced resistivity remains after annealing at 300 K. During annealing at higher temperature the resistivity anneals out completely at about 600 K.
- The proton irradiated Fe-C samples exhibit a slightly higher retained resistivity at 300 K, 8-11%. After a sharp recovery stage at IV_A at 330 K the retained resistivity is comparable to that of pure Fe.
- At higher annealing temperature the irradiated Fe-C samples exhibit another recovery stage, IV_B, at 550-600 K, where the resistivity drops below the pre-irradiation value.
- The observations are attributed to the interaction of C with irradiation defects to form defect complexes. Most probably these complexes are vacancy-C clusters. The presence of these clusters retards the process of carbide formation.

- The stage A observed in un-irradiated samples is absent in the irradiated ones. This is because carbon atoms are trapped in the irradiation-induced defects and are not available to form the metastable ε-carbide at 440 K, as it happens in the un-irradiated specimens.
- Stage B observed in un-irradiated speciments is the same as IV_B in the case of irradiated samples and is due to precipitation of cementite. At high irradiation dose IV_B shifts to higher temperature ($\sim$ 600 K). This is attributed to the higher concentration of irradiation defects, which in turn results in higher numbers C atoms participating in vacancy-C clusters. This retards the process of cementite precipitation and thus it occurs at higher temperature.

Bibliography

[1] D. M. Duffy. Fusion power: a challenge for materials science. *Phil. Trans. R. Soc. A*, 368:3315–3328, 2010.

[2] J. Knaster, Moeslang A., and T. Muroga. Materials research for fusion. *Nature Physics*, 12(10):424, May 2016.

[3] R. A. Forrest, A. Tabasso, C. Danani, S. Jakhar, and A. K. Shaw. *Handbook of activation data calculated using EASY-2007*. EURATOM/UKAEA Fusion Association, 2009.

[4] N. Baluc, R. Schaeublin, Spaetig P., and Victoria M. On the potentiality of using ferritic/martensitic steels as structural materials for fusion reactors. *Nucl. Fusion*, 44:56, 2004.

[5] G. H. Vineyard and G. J. Dienes. *Radiation effects in solids*. Interscience Publishers, Inc., New York, 1957.

[6] William D. Jr. Callister and David G. Rethwisch. *Fundamentals of materials science and engineering*. Wiley, 2012.

[7] Peter Atkins and Julio de Paula. *Physical Chemistry*. Oxford University Press, 2006.

[8] Clemens J. Foerst, Jan Slycke, Krystyn J. Van Vliet, and Sidney Yip. Point defect concentrations in metastable fe-c alloy. *Physical Review Letters*, 96:175501, May 2006.

[9] John D. Verhoeven. *Steel Metallurgy for the Non-Metallurgist*. ASM International, 2007.

[10] H. K. D. H. Bhadeshia and Sir Robert Honeycombe. *Steels, Microstucture and Properties*. Elsevier, 2006.

[11] H. Okamoto. The carbon-iron system. *Journal of Phase Equilibria*, 13:543, 1992.

[12] J. Le Coze. *Final Report on Model Alloy Preparation*. 2007.

[13] Robert W. Messler. *Principles of Welding*. Wiley, 1999.

[14] Viktoria Lukianova. *Short-Range Order (SRO) Kinetics in Fe-Cr Alloys studied by means of Electrical Resistivity Measurements*. 2013.

[15] J.G. Ziegler and N.B. Nichols. *Optimum Settings for Automatic Controllers*. 1942.

[16] R. Hellborg. *Electrostatic Accelerators, Fundamentals and Applications*. Springer, 2005.

[17] Zoi Kotsina. *Radiation Damage studies of Proton Irradiated Fe-Cr Alloys by Electrical Resistivity Measurements*. 2016.

[18] David R. Lide. *CRC Handbook of Chemistry and Physics*. 2007.

[19] H. Wagenblast and Sigurds Arajs. Electrical resistivity of iron-carbon alloys. *Journal of Applied Physics*, 39:5885, December 1968.

[20] P. Jung, P. Ehrhart, and H. Schultz. *Atomic Defects in Metals*. Landolt-Börnstein - Group III Condensed Matter 25 : Condensed Matter. Springer-Verlag Berlin Heidelberg, 1 1991.

[21] F. E. Fujita and A. C. Damask. Kinetics of carbon precipitation in irradiated iron-ii electrical resistivity mesurements. *Acta Metllurgica*, 12:331–339, 1964.

[22] S. Takaki, H. Kimura, and T. Kimura. The resistivity recovery of high purity and carbon-doped iron after low and room temperature deformation. *Material Science Forum*, 15-18:691–696, 1987.

[23] Michel Perez and Alexis Deschamps. Microscopic modelling of simultaneous two-phase precipitation: application to carbide precipitation in low-carbon steels. *Materials Science and Engineering: A*, 360(1–2):214–219, 1 2003.

[24] S. Takaki, J. Fuss, H. Kuglers, U. Dedek, and H. Schultz. The resistivity recovery of high purity and carbon doped iron following low temperature electron irradiation. *Radiation Effects and Defects in Solids*, 79:87–122, December 1983.